Marcus-Hush Theory Revealed by Electron Tunneling Through Hexagonal Boron Nitride

Matěj Velický,*[1,2,3] Sheng Hu,[2] Colin R. Woods,[2] Peter S. Toth,[1,4] Viktor Zólyomi,[2] Andre K. Geim,[2] Héctor D. Abruña,[3] Kostya S. Novoselov,[2] and Robert A. W. Dryfe*[1]

[1] School of Chemistry and [2] School of Physics and Astronomy, University of Manchester, Oxford Road, Manchester, M13 9PL, United Kingdom
[3] Department of Chemistry and Chemical Biology, Cornell University, Ithaca, New York, 14853, United States
[4] MTA Premium Post Doctorate Research Program, Department of Physical Chemistry and Materials Science, University of Szeged, Rerrich Square 1, Szeged H-6720, Hungary

ABSTRACT

Marcus-Hush theory of electron transfer is one of the pillars of modern electrochemistry with a large body of supporting experimental evidence presented to date. However, some predictions, such as the electrochemical behavior at microdisk electrodes, remain unverified. Herein, we present a study of electron tunneling across a hexagonal boron nitride barrier between a graphite electrode and redox levels in a liquid solution. This was achieved by the fabrication of microdisk electrodes with a typical diameter of 5 μm. Analysis of voltammetric measurements, using two common redox mediators, yielded several electrochemical parameters, including the electron transfer rate constant, limiting current, and transfer coefficient. They show a significant departure from the Butler-Volmer behavior in a clear manifestation of the Marcus-Hush theory of electron transfer. In addition, our system provides a novel experimental platform, which could be applied to address a number of scientific problems such as identification of reaction mechanisms, surface modification, or long-range electron transfer.

INTRODUCTION

Marcus-Hush theory has long been recognized as the most successful attempt at developing a comprehensive model of electron transfer kinetics.[1-2] It describes the electron transfer between reactants and products as a temperature-activated process governed by nuclear vibrations, energy reorganization, and electronic coupling. Several experimental confirmations of this theory have emerged since its inception in the 1950s, notably the observation of the so-called inverted region for intramolecular electron transfer[3] and flattening of the exponential dependence of the rate constant on potential for electrode reactions.[4] However, some intriguing predictions from the Marcus-Hush theory exist, which have not yet been observed experimentally. This includes the voltammetric behavior at inlaid microdisk electrodes, put forth by Feldberg, who predicted peculiar deviations of the steady-state voltammograms from the commonly-used Butler-Volmer model of electrochemical kinetics.[5]

Hexagonal boron nitride (hBN) is arranged into two-dimensional (2D) layers, in which boron and nitrogen atoms are covalently bound in an alternating hexagonal pattern, similar to graphene. These layers are held together by van der Waals (vdW) forces in bulk hBN. The lattice mismatch between hBN and graphene is only 1.5%,[6-7] their bulk interlayer spacing is nearly identical (3.3–3.4 Å),[7-8] and its polar nature renders hBN insulating, with a wide band gap of ~6 eV.[9-10] These characteristics lead to an increased carrier mobility in graphene supported or encapsulated by hBN, owing to the atomic flatness, lack of dangling bonds, and suppression of charge doping at the graphene/hBN interface.[11-13] It transpires from the present work that hBN is a suitable medium to study long-range electron tunneling, which leads to the observation of the Marcus-Hush behavior.

The quantum tunneling effect is a direct consequence of the Heisenberg uncertainty principle and is most pronounced for light particles, such as electrons, whose de Broglie wavelength is comparable to the tunneling distance.[14] Initially discovered for trapped electrons,[15] long-range electron tunneling gradually defined many diverse research fields including scanning tunneling microscopy, molecular electronics, and DNA sequencing.[16-17] A significant body of the electrochemical tunneling studies have involved the following two approaches of modifying conducting electrodes: self-assembled monolayers of redox species tethered to an insulating alkyl chain, or insulating polymer films with a redox mediator in solution.[18] hBN provides an inorganic alternative with a precise control of the tunneling distance, especially within the subnanometer regime, unattainable even for the state-of-the-art tunneling layers of Al_2O_3 grown by atomic layer deposition at thicknesses of ~1 nm.[19] Additionally, the high crystallinity of hBN and short barrier length ensure scattering-free ballistic electron tunneling and therefore no ohmic heating within the dielectric.[17] It is therefore not surprising that hBN has been utilized as a tunneling barrier in solid state devices. This has included hBN being sandwiched between two metals, two graphene/graphite layers, and a metal and graphene.[20-24] Most of these studies found that the tunneling current increases exponentially with the applied voltage and decays exponentially with the hBN thickness to negligible levels for ~6-layer hBN. Both experiments and theory suggest that hBN is not simply a passive insulating barrier but rather that it affects the tunneling through carrier interactions with phonons, defects, and dopants.[23-25]

Herein, we employ atomically-flat hBN as a tunneling barrier to an electrochemical reaction between a redox mediator in a liquid solution and a graphite electrode (Figure 1). We make use of electron-beam (e-beam) lithography to fabricate inlaid disk ultramicroelectrodes and employ a modified microdroplet electrochemical cell technique, described elsewhere.[26] The use of

a high-quality, crystalline 2D insulator has some advantages over the two traditional tunneling approaches described above, owing to the chemically inertness of hBN, the lack of dangling bonds on its basal plane surface, and a microscopic size of the tunneling area. These characteristics lead to an atomically-flat electrode surface, well-defined control of the tunneling distance *via* the number of hBN layers (*N*), significant reduction in the occurrence of pinholes and defects, and 'simplicity' of an inorganic tunneling barrier, contrasting with the complexity of organic barriers, which possess discrete molecular energy levels and specific chemical interactions. The steady-state voltammograms of $[IrCl_6]^{3-}$ oxidation and $[Ru(NH_3)_6]^{3+}$ reduction in this system exhibit the expected exponential dependence of the electron transfer rate on the tunneling distance for monolayer (1L) and bilayer (2L) hBN. However, significant deviations in the measured electrochemical parameters are observed for thicker hBN due to the manifestation of the Marcus-Hush theory. We further rationalize the results based on the density functional theory (DFT) calculations of the energy levels in the graphite/hBN/liquid heterostructure.

EXPERIMENTAL SECTION

Device Fabrication and Characterization

The tunneling devices were prepared by mechanical exfoliation of graphite (NGS Naturgraphit) and hBN (hq graphene), dry stamp-transfer, and e-beam lithography (Zeiss EVO), as described in Supporting Fig. S1. Briefly, graphite was exfoliated to *ca*. 10–30 nm thickness onto a 300 nm SiO_2/Si substrate. hBN was exfoliated onto poly(methyl methacrylate) PMMA substrate and then placed on the graphite using the stamp-transfer method.[27] The resulting hBN/graphite heterostructure was spin-coated with an insulating PMMA layer (130 nm thick), in which two identical circular working electrode openings (typically 5 μm in diameter) over the basal planes of bare graphite and hBN were created using e-beam lithography (Fig. 1a–b). Electrical contact was made by scratch-exposing the graphite away from the openings and bonding it to a Cu wire using Ag paint. A Nikon Eclipse LV100ND optical microscope and a DS-Fi2 U3 CCD camera (Nikon Metrology, UK Ltd) were employed to acquire the optical images (Fig. 1c–d). The electrochemical cell was formed by dispensing a microdroplet of a liquid solution (typically 60–100 μm in diameter) around the opening (Fig. 1e). The number of hBN layers was determined by a Bruker Dimension 3100V atomic force microscope (AFM) in tapping mode (Fig. 1f). Raman spectra were collected using an inVia spectrometer (Renishaw) with a 532 nm laser excitation and X-ray photoelectron spectroscopy (XPS) was measured using a Thermo Scientific Al K-Alpha Theta Probe.

Electrochemical Measurements

All electrochemical measurements were performed in 6 M LiCl supporting electrolyte aqueous solution, which minimized the evaporation of the liquid. Dispensation and manipulation of the microdroplets on the surface was controlled using a pneumatic microinjector and a

micromanipulator reported previously.[26, 28] The potential (E) was applied to the graphite electrode using a PGSTAT302N potentiostat (Metrohm Autolab) and a scan rate of 100 mV s^{-1} was used in order to achieve a steady-state ultramicroelectrode response without thin-layer cell diffusional effects (Supporting Fig. S2). The standard heterogeneous electron transfer rate constant (k^0), limiting current density (j_{lim}), and transfer coefficient (α or $1-\alpha$) were determined by fitting the voltammograms with an empirical function using equations (10), (11) and (13) in ref. [29], derived based on the Butler-Volmer model of electrochemical kinetics. The diffusion coefficients of 2.5 (2.2) $\times$ 10^{-6} cm^2 s^{-1} for the oxidized (reduced) form of [Ru(NH$_3$)$_6$]$^{3+/2+}$ and 2.4 (2.1) $\times$ 10^{-6} cm^2 s^{-1} for the oxidized (reduced) form of [IrCl$_6$]$^{2-/3-}$, were determined as averages from cyclic voltammetry and chronoamperometry at a Pt disk electrode (1.1 mm radius) using the Randles-Ševčík and Cottrell equations, respectively.[18] The formal potentials ($E^{0'}$) of [Ru(NH$_3$)$_6$]$^{3+/2+}$ and [IrCl$_6$]$^{2-/3-}$ reduction/oxidation were determined from cyclic voltammetry using the same electrode. The potential, measured against an Ag/AgCl reference electrode, was converted to the standard hydrogen electrode (SHE) scale. A large-area Pt counter electrode was used to complete the three-electrode configuration. All measurements were carried out at ambient temperature (20–25 ºC).

DFT Calculations

Theoretical calculations were performed using the VASP code[30] in a plane-wave basis. Bulk graphite was approximated with a 6L thick slab. We used a plane-wave cutoff energy of 600 eV throughout and left at least 20 Å of vacuum space above the 2D sheets in order to model isolated materials. The k-point grid was set to a Γ-centered 12×12×1 Monkhorst-Pack grid. The local density approximation was used to compute the band structures, ionization energies, and hBN band gaps. A correction to the latter quantities was necessary as both of them are underestimated in

semi-local DFT.[31] The scissor correction to the band gap and correction to the ionization energy were obtained by recalculating these quantities in the few-layer ($\leq$ 3L) limit of hBN using the HSE06 functional.[32] We found no dependence of either correction on N and therefore assume that it can be applied to all hBN thicknesses.
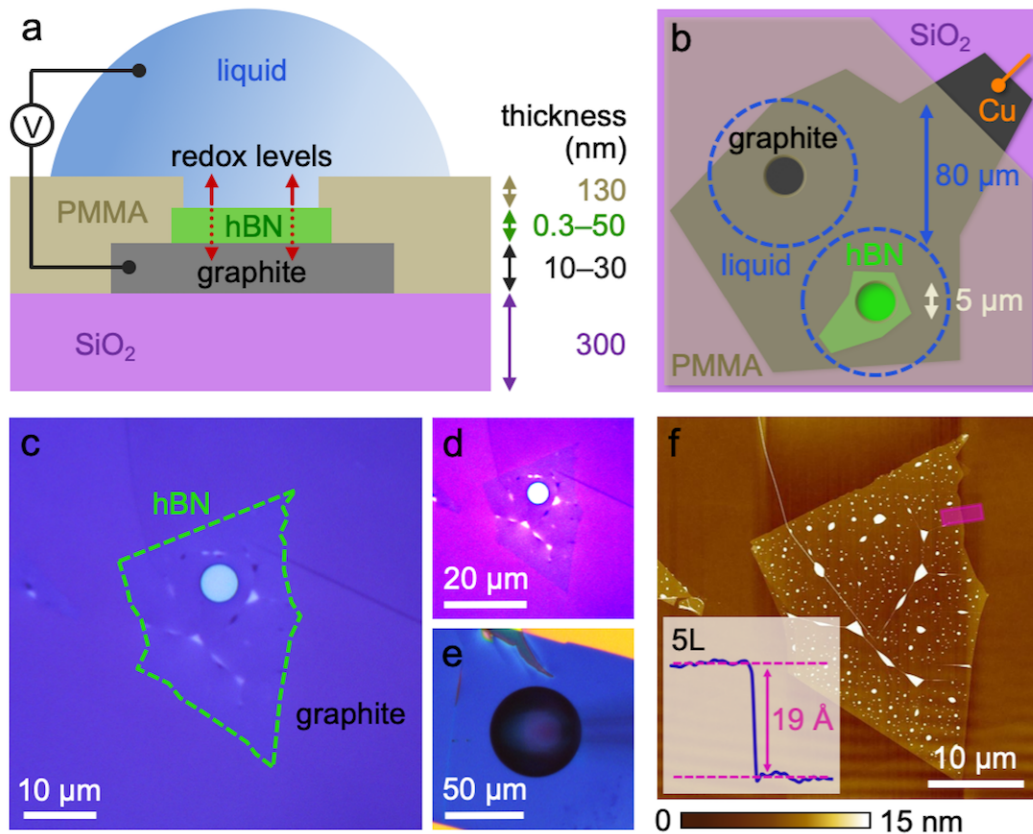
Figure 1 │ Schematics and Characterization of the hBN Tunneling Devices. a–b, Side- and top-view schematics of the tunneling device, respectively. **c,** Optical image of the PMMA/hBN/graphite/SiO$_2$ heterostructure. **d,** Same as **c** but in false color and contrast-enhanced. **e,** Liquid microdroplet electrochemical cell on the same device, injected via a glass capillary (shadow on the right). **f,** AFM characterization of hBN on graphite prior to the e-beam lithography with the step-edge profile shown in the inset.

RESULTS

Anatomy of the Tunneling Device

The electron tunneling from (to) the redox mediator in the liquid phase, through hBN of varied thickness, to (from) the graphite electrode was realized using devices depicted in Fig. 1a–b. The basal planes of both graphite and hBN have planar sp^2 hybridization, are chemically inert, and lack dangling bonds. Crucially, their surfaces, which face each other in the resulting heterostructure, are not exposed to any polymer or solvent during the assembly. This ensures that the interface between these two materials is well-defined and atomically-flat and that the tunneling distance between the redox mediator and graphite can be controlled by the number of hBN layers. In reality, we do observe some contaminants trapped between the hBN and graphite, which favorably agglomerate in micro/nanoscopic pockets visible in AFM (Fig. 1f), due to the self-cleaning process occurring at the vdW interfaces.[33] Importantly, the average height of these pockets is at least 5 nm, leading to a negligible overlap between the electron wave functions of the redox mediator and graphite,[17] which therefore only results in a mere reduction of the apparent tunneling area.
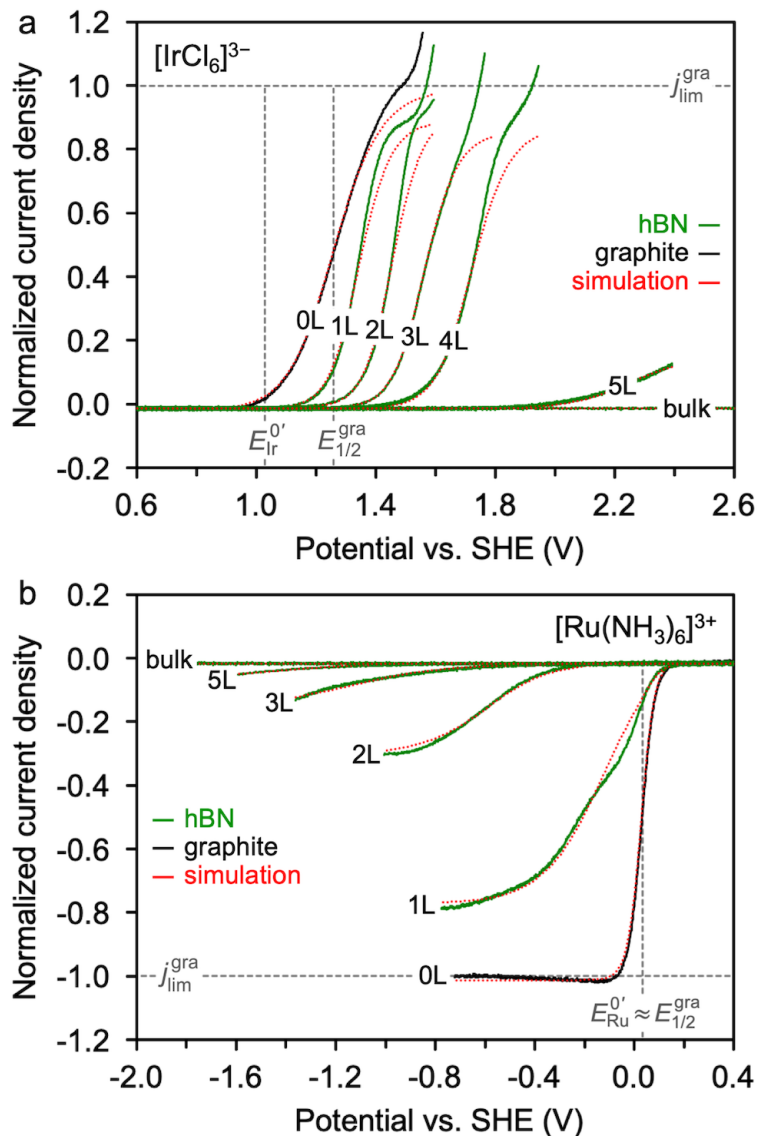
Voltammetry of the Electron Tunneling Through hBN

The electron tunneling through hBN in the graphite/hBN/liquid heterostructure was measured by voltammetry, *i.e.* a current-voltage measurement, and is summarized in Fig. 2. The tunneling process is driven by the difference between the energy of the $[IrCl_6]^{2-/3-}$ or $[Ru(NH_3)_6]^{3+/2+}$ redox levels ($E_{Ir}^{0'}$ or $E_{Ru}^{0'}$) in the liquid and the Fermi level (E_F) of graphite, to which positive or negative potentials are applied, respectively. As a result, $[IrCl_6]^{3-}$ or $[Ru(NH_3)_6]^{3+}$ are oxidized or reduced to $[IrCl_6]^{2-}$ or $[Ru(NH_3)_6]^{2+}$ and positive or negative currents are recorded, respectively. Voltammograms on the bare graphite, labeled as 0L in Fig. 2, were also recorded as a control.

The voltammograms of $[IrCl_6]^{3-}$ oxidation in Fig. 2a exhibit the steady-state sigmoidal shape expected for disk ultramicroelectrodes, for both the bare graphite (black curve) and hBN layers (green curves). However, rather than maintaining the limiting value of the potential-independent plateau, the current density rises further at large positive potentials, owing to the graphite oxidation side-reaction delimiting the potential window. All hBN voltammograms maintain a similar shape to that of the bare graphite, but are offset to increasingly more positive potentials upon increasing N. The red curves, fitted to the voltammograms using an empirical function described in ref [29], allowed us to extract k^0, j_{lim}, and $(1-\alpha)$ or α. The k^0 of $[IrCl_6]^{3-}$ oxidation on bare graphite ($\overline{k^{0,\,gra}}$) averaged over all the devices was $(1.4 \pm 0.2) \times 10^{-3}$ cm s^{-1}, about one order of magnitude lower than reported previously,[34] not entirely unexpected considering the exposure of the topmost surface to PMMA during device fabrication.

Interestingly, the partial oxidation of graphite, observed at large positive potentials in voltammograms of Fig. 2a, left the consecutive $[IrCl_6]^{3-}$ voltammograms unaffected, but had notable implications for the subsequent $[Ru(NH_3)_6]^{3+}$ voltammetry. The $[Ru(NH_3)_6]^{3+}$ reduction

voltammograms shown in Fig. 2b are qualitatively similar to those of $[IrCl_6]^{3-}$ in that they exhibit the sigmoidal steady-state behavior and the hBN curves occur at increasingly more negative potentials as the hBN thickness increases. However, the k^0 values are much higher than expected. Specifically, the $\overline{k^{0,\,gra}}$ of $[Ru(NH_3)_6]^{3+}$ reduction averaged over all the devices was $(9.5 \pm 2.0) \times 10^{-2}$ cm s^{-1}, which is 3–4 orders of magnitude higher than reported previously,[34] and close to value observed for laser-activated graphite.[35] This indicates that mild oxidation introduces sp^3 disorder in the graphitic lattice and leads to an increase in the density of electronic states (DOS) near the E_F of unbiased graphite (E_F^0), which lies within 0.05 eV of $E_{Ru}^{0\prime}$.[36] We recognize that such effects render our analysis semi-quantitative, and as such, our main aim is to expose qualitative trends, rather than to obtain absolute values of electrochemical quantities. The evolution of the voltammetric background with N in the pure supporting electrolyte is detailed in Supporting Fig. S3.

Figure 2 | Voltammetry of Electron Tunneling Through hBN. a–b, Steady-state voltammograms of $[IrCl_6]^{3-}$ oxidation and $[Ru(NH_3)_6]^{3+}$ reduction, respectively, on hBN (green curves) and bare graphite (black curves), recorded at scan rate of 100 mV s^{-1}. The current density is normalized to the limiting current density of graphite (j_{lim}^{gra}). Bulk corresponds to 26 hBN layers (9 nm). The curves were fitted with an empirical function (red) to obtain the electrochemical parameters, as detailed in the Experimental Section.

Dependence of the Electron Transfer Rate on Tunneling Distance

Figure 3 shows the measured rate constants as a function of the tunneling distance. It is evident from Fig. 3a that k^0 of $[IrCl_6]^{3-}$ and $[Ru(NH_3)_6]^{3+}$, albeit different in absolute value, both decay with the hBN thickness. This is in qualitative agreement with both experiments and predictions for coherent quantum tunneling.[16] The exponential dependence of the electron transfer rate constant between an electrode and redox species (k_{ET}, in s^{-1}) on the tunneling distance between the two (x) is described as:[18]

$$k_{ET}(x) = k_{ET}(0)\, e^{-\beta x} \tag{1}$$

where $k_{ET}(0)$ and $k_{ET}(x)$ are the k_{ET} values at the electrode surface ($x = 0$) and at the distance x from it, respectively, and β is the tunneling decay coefficient. Studies of electron tunneling using redox centers tethered to organic molecules with typical lengths of 5–50 Å on metal electrodes revealed β values of 1.0–1.2 Å^{-1} for alkanethiol chains,[37-38] 0.4–0.6 Å^{-1} for π-conjugated chains,[39-40] and 0.2–0.3 Å^{-1} for aromatic chains.[41-43] Tunneling through vacuum between two metals typically yields β values of 2.0–2.5 Å^{-1}.[18]

Consequently, one could be tempted to perform a linear fit of data in Fig. 3a by adopting Eq. (1) for k^0. Doing so would yield β of 0.4–0.5 Å^{-1}, which is somewhat smaller than expected for a wide bandgap insulator. In fact, it is evident from Fig. 3a that the distance dependence of $\ln(k^0)$ is not linear and decays more slowly as x increases, as seen for $\geq$ 3L hBN. When only 1L and 2L hBN are considered for the linear fit, reasonable β values of 1.2 Å^{-1} and 1.1 Å^{-1} for $[IrCl_6]^{3-}$ and $[Ru(NH_3)_6]^{3+}$ are obtained. The deviation from Eq. (1) at large x becomes very apparent when the data are normalized to $\overline{k^{0,\,gra}}$, as shown in Figs. 3b and 3c. Plotted this way, the linear fit ought to pass near the origin, since, by definition, for $x = 0$ the argument of the natural logarithm is 1. Indeed, when 0L, 1L, and 2L data are considered for the linear fit in Fig. 3b–c, β values of 1.1 Å$^-$

^{1} and 1.0 Å^{-1} for $[IrCl_6]^{3-}$ and $[Ru(NH_3)_6]^{3+}$ are obtained and the fitted lines pass within $\pm$ 0.2 Å

from the origin. This data normalization also has the noteworthy advantage of canceling out the

effects of solvent, electrolyte, and impurity adsorption at the electrode surface.

Let us now review the quantitative aspects of electron transfer formalized by Marcus-Hush

theory. The following formalism for k_{ET} is usually invoked, describing the electron transfer as a

temperature-activated process:[44-46]

$$k_{ET} = v_n \kappa_{el} \kappa_n \tag{2}$$

where v_n is the effective nuclear vibration frequency, κ_{el} is the electronic transmission coefficient,

and κ_n is the nuclear reorganization factor, typically expressed in terms of the standard free energy

of activation ($\Delta G^{\ddagger}$):[18]

$$\kappa_n = e^{-\frac{\Delta G^{\ddagger}}{k_B T}} \tag{3}$$

where k_B is the Boltzmann constant and T is the temperature. Of all the above quantities, κ_{el} is the

only source of the exponential decay with distance:

$$\kappa_{el}(x) = \kappa_{el}(0) e^{-\beta x} \tag{4}$$

where $\kappa_{el}(0)$ and $\kappa_{el}(x)$ are the κ_{el} values at the electrode surface ($x = 0$) and at a distance x from it,

respectively. In the adiabatic regime of strong electronic coupling, $\kappa_{el}(x) \rightarrow 1$, which manifests

itself by the independence of the rate constant on distance.[38] At larger distances, the electronic

coupling weakens, $\kappa_{el}(x) < 1$, and even an initially adiabatic reaction becomes non-adiabatic and

independent of the nuclear dynamics since $\kappa_{el}(x)$ is reduced to:[44, 46-47]

$$\kappa_{el}(x) = \frac{v_{el}^0}{v_n} e^{-\beta x} \tag{5}$$

where v_{el}^0 is the electron hopping frequency at $x = 0$. This quantity is a function of the electrode DOS (ρ_E^0) at energy corresponding to $E^{0'}$ and the electronic coupling matrix between the electrode and redox states (H_{ER}^0) at $x = 0$, according to the Landau-Zener formalism:[44, 48]

$$v_{el}^0 = \frac{4\pi^2 \rho_E^0 \left(H_{ER}^0\right)^2}{h\sqrt{4\pi\frac{\lambda}{k_B T}}} \tag{6}$$

where h is the Planck constant and λ is the reorganization energy of the redox mediator. Many outer-sphere electrode reactions are non-adiabatic due to weak electronic coupling, which also applies to our system as a result of the low DOS of graphite.[36, 49] The standard heterogeneous electron transfer rate constant k^0 (in cm s^{-1}) is a special case of k_{ET} at $E = E^{0'}$, integrated over all the distances from the electrode, so from Eq. (2) we have:

$$k^0 = \int_{x=0}^{\infty} k_{ET}\left(E = E^{0'}\right)dx = v_n \kappa_n \left(E = E^{0'}\right) \int_{x=0}^{\infty} \kappa_{el}\, dx \tag{7}$$

Feldberg and Sutin derived an expression for k^0 for non-adiabatic reactions at electrode surfaces,[44] which in combination with Eq. (1) finally yields the distance dependent k^0:

$$k^0(x) = \frac{v_{el}^0}{\beta} \frac{\pi}{\sqrt{1 + \frac{\pi k_B T}{\lambda}}} e^{-\frac{\lambda}{4 k_B T}} e^{-\beta x} \tag{8}$$

When the coherent quantum tunneling arises solely from the electronic coupling between the electrode and the redox mediator, then β exclusively describes the tunneling decay, is independent of potential and temperature, and its inverse has the physical meaning of a reaction zone thickness.[45]

Eq. (8) provides the means to estimate v_{el}^0 from the intercepts in Fig. 3a. Using an arbitrary value of $\lambda = 1.0$ eV for both mediators[50] yields v_{el}^0 of 6.8×10^7 s^{-1} and 2.3×10^{11} s^{-1} for $[IrCl_6]^{3-}$ and $[Ru(NH_3)_6]^{3+}$, respectively. We then use these v_{el}^0 values and Eq. (6) to calculate ρ_E^0 at $x = 0$,

i.e. the DOS of the bare graphite (assuming $H_{ER}^0 \approx 0.1$ eV).[44] The ρ_E^0 of 1.6×10^{-5} atom^{-1} eV^{-1} for

$[IrCl_6]^{3-}$ is in agreement with recently determined values for basal plane graphite, while the ρ_E^0 of

5.4×10^{-4} atom^{-1} eV^{-1} for $[Ru(NH_3)_6]^{3+}$ is closer to the edge plane of graphite, consistent with the

above discussion.[36]
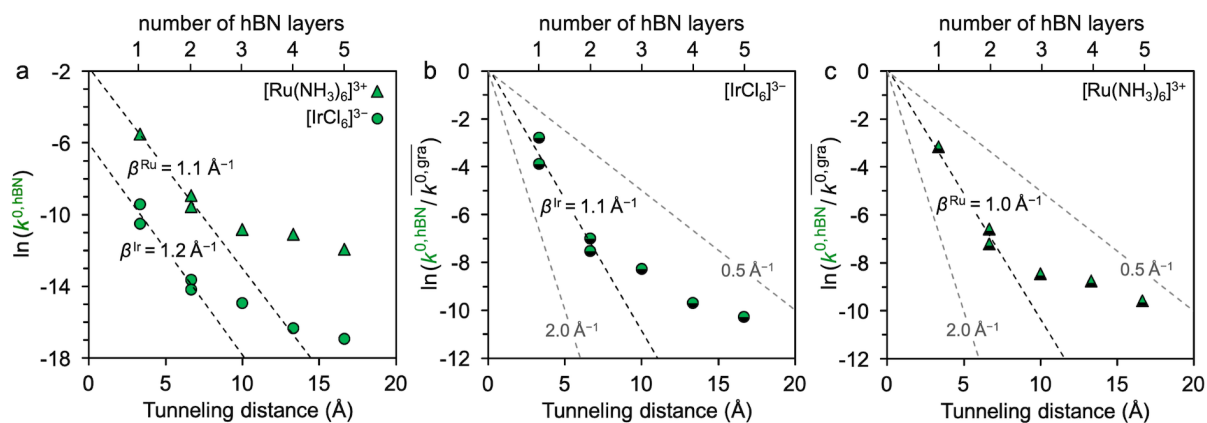
Figure 3 | Dependence of the Electron Transfer Rate on Tunneling Distance. a, Natural logarithm of the standard heterogeneous electron transfer rate constant ($k^{0,\mathrm{hBN}}$) as a function of the tunneling distance for $[\mathrm{IrCl_6}]^{3-}$ (circles) and $[\mathrm{Ru(NH_3)_6}]^{3+}$ (triangles). The same dependence with $k^{0,\mathrm{hBN}}$ normalized to $\overline{k^{0,\mathrm{gra}}}$ is shown in **b** for $[\mathrm{IrCl_6}]^{3-}$ and in **c** for $[\mathrm{Ru(NH_3)_6}]^{3+}$. β values are determined from the regression lines fitted to the 1–2L data in **a** and 0–2L data in **b–c**, and dependencies corresponding to β of 2.0 Å^{-1} and 0.5 Å^{-1} are plotted in **b–c** for comparison. The tunneling distance was calculated from N using the theoretical vdW spacing (3.3 Å) in bulk hBN.[8]

Observation of the Marcus-Hush Theory of Electron Transfer

We observe further anomalies in the other two electrochemical parameters determined from the voltammetric fitting, namely the transfer coefficient and limiting current density, which are plotted in Figure 4 as a function of the tunneling distance. Fig. 4a and 4 b indicate an average $(1-\alpha)$ of 0.36 for $[IrCl_6]^{3-}$ and α of 0.58 for $[Ru(NH_3)_6]^{3+}$, both of which are reasonable values, indicating a high symmetry of the reduction/oxidation reactions.[18] However, a progressive decrease of an initially constant $(1-\alpha)$ of 0.51 is observed for $[IrCl_6]^{3-}$ oxidation for >3L hBN. $[Ru(NH_3)_6]^{3+}$ reduction on hBN does not exhibit as clear a decrease in α with the tunneling distance but yields unusually small values of α between 0.13 and 0.27. Another striking observation shown in Fig. 4c and 4c is that the normalized j_{lim} does not reach the expected unity maximum at large potentials and instead decreases progressively with increasing tunneling distance. This is true for $[IrCl_6]^{3-}$ with 5L hBN, and for $[Ru(NH_3)_6]^{3+}$ with all hBN thicknesses. The small <15% decrease in $[IrCl_6]^{3-}$ j_{lim} on 1–4L hBN can be attributed to the previously discussed contamination at the hBN/graphite interface.

Such anomalous behavior of j_{lim} and α (or $1-\alpha$) indicates a departure from the Butler-Volmer model of electrochemical kinetics, which was used to analyze the data. In a predictive theoretical study, Feldberg showed that, under certain conditions, the steady-state voltammograms on disk ultramicroelectrodes deviate from the Butler-Volmer behavior and instead follow the Marcus-Hush theory.[5] Crucially, the Butler-Volmer model continues to produce a good voltammetric fit but k^0 and α (or $1-\alpha$) become mere fitting parameters. Consequently, their apparent values increase and decrease, respectively, and the physical value of j_{lim} decreases as Marcus-Hush behavior dominates, much in agreement with our observations. The qualitative conditions necessary to observe these anomalies were identified as: large potentials, small k^0, small

electrode size, and small λ, *i.e.* "fast" redox systems. Feldberg argued that such conditions are difficult to achieve simultaneously in an experiment,[5] but fortuitously, our experimental system favorably meets all of these conditions. For $\lambda = 1.0$ eV, the two kinetics models are only distinguishable when $|E - E^{0'}| \geq 0.5$ V (easily accessible in our system), and 99% of the Marcus-Hush potential-independent k^0 plateau is reached when $|E - E^{0'}| \geq 1.5$ V.[5] Furthermore, the following distinguishability condition must be met:

$$\frac{k^0 r}{D} \leq 10^{\left(1 - \frac{\lambda}{10\,k_\mathrm{B}T}\right)} \tag{9}$$

where r is the electrode radius and D is the diffusion coefficient of the redox mediator. One way to approach this condition is to decrease r to units of nanometers, a feat demonstrated more than a decade ago,[51] however, this leads to complications since r becomes comparable to the electrical double layer thickness. Basal plane graphite has long been identified as having small k^0 for outer-sphere redox mediators, due to its low DOS, but little effort has been expended toward employing it as an ultramicroelectrode. More crucially, very few systems have values of k^0 and λ low enough to meet the conditions imposed by Eq. (9), since k^0 increases with decreasing λ, according to Eq. (8). Our system is unique, since λ is kept constant, whereas k^0 decreases progressively with the tunneling distance due to the weakened electronic coupling. Consequently, the combination of basal plane graphite ultramicroelectrodes with $r = 2.5$ μm and tunneling through hBN, which pushes the apparent k^0 to below 10^{-7}–10^{-5} cm s^{-1}, allows the conditions imposed by Eq. (9) to be met, subject to the value of λ. In fact, we can obtain a rough estimate of λ, based on the observed deviation from the expected exponential decay between 2–3L hBN layers (Fig. 3). Indeed, evaluating k^0, r, and D values against Eq. (9) leads to $\lambda \approx 1.3$ eV for $[\mathrm{IrCl_6}]^{3-}$ and $\lambda \approx 0.7$ eV for $[\mathrm{Ru(NH_3)_6}]^{3+}$, both in agreement with experimentally determined values of ~1.2 eV[52] and ~0.6 eV[53], respectively, although in disagreement with theoretical predictions.[50] This also explains why

deviations in α and j_{lim} are only seen at the largest distances for $[\text{IrCl}_6]^{3-}$ while anomalous behavior is observed for $[\text{Ru(NH}_3)_6]^{3+}$ across the entire range of distances. We stress that the above evaluation is very approximate and does not fully explain all the aspects of the observed deviations.
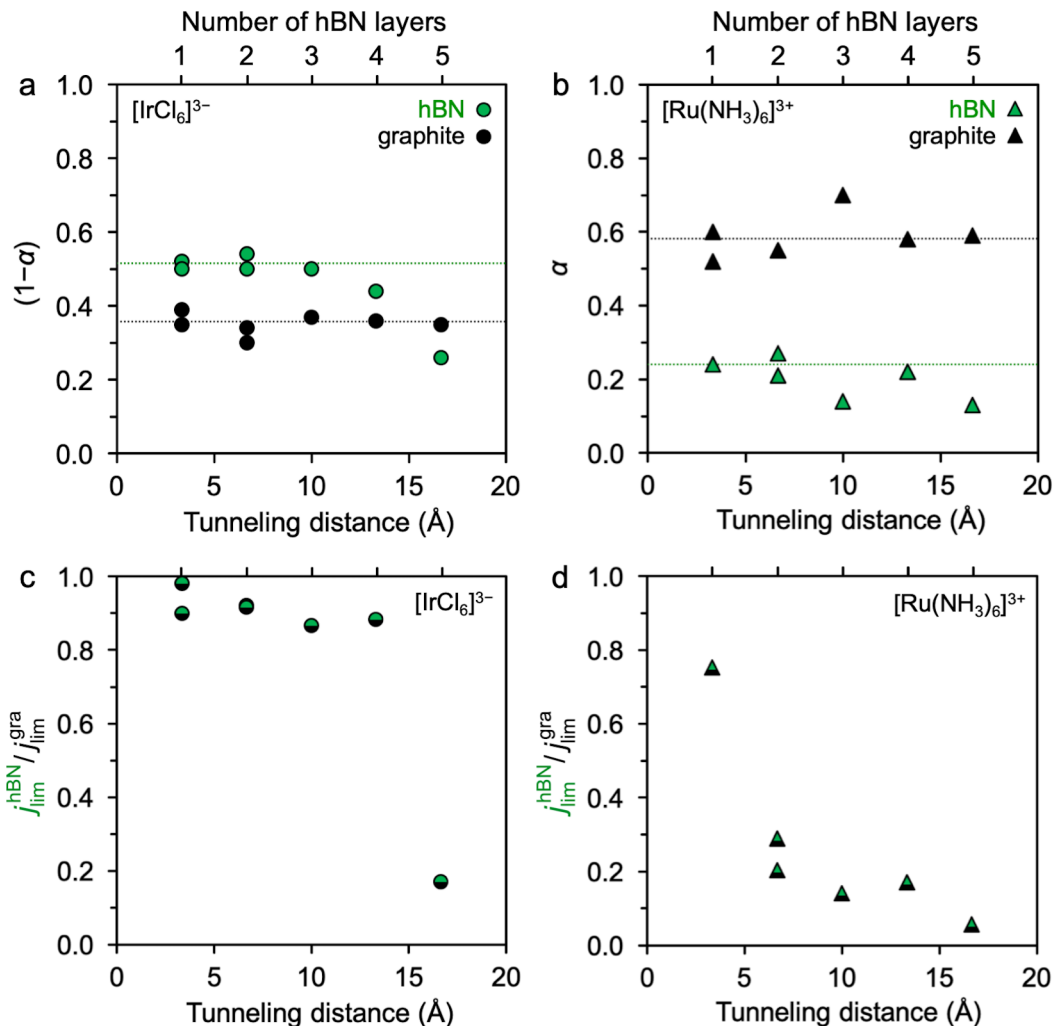
Figure 4 | Dependence of the Transfer Coefficient and Limiting Current Density on Tunneling Distance. a–b, $(1-\alpha)$ and α as a function of the tunneling distance for $[\text{IrCl}_6]^{3-}$ and $[\text{Ru(NH}_3)_6]^{3+}$, respectively. Green marks correspond to hBN, black ones to bare graphite. **c–d,** Limiting current density on hBN $(j_{\text{lim}}^{\text{hBN}})$ as a function of the tunneling distance for $[\text{IrCl}_6]^{3-}$ and $[\text{Ru(NH}_3)_6]^{3+}$, respectively, normalized to the limiting current density on bare graphite $(j_{\text{lim}}^{\text{gra}})$.

Properties of the hBN Tunneling Barrier

It is instructive to consider the properties of the tunneling barrier and its dependence on the hBN thickness and applied potential. The band diagram in Fig. 5a schematically depicts the various energy levels in the graphite/1L hBN/liquid heterostructure and their mutual alignment for the unbiased case prior to contact between the three phases. Fig. 5b shows the tunneling process for the $[IrCl_6]^{3-}$ oxidation, with a large positive potential applied to the graphite allowing the electrons to tunnel from the occupied states of $[IrCl_6]^{3-}$ to the empty states in graphite. Similarly, Fig. 5c shows the electron tunneling from the occupied states in graphite to the empty states of $[Ru(NH_3)_6]^{3+}$, facilitated by the large negative potential applied to the graphite. An important implication of the analysis in Figs. 5a-c is that both processes are dominated by the electron/hole tunneling near the valence band maximum (VBM), rather than the conduction band minimum (CBM), of hBN, since this path has a significantly lower tunneling barrier. Furthermore, the barrier for tunneling to/from $[IrCl_6]^{3-}$ is smaller than that for $[Ru(NH_3)_6]^{3+}$ thanks to the relative position of the redox levels and VBM of hBN.

The dependence of the hBN band structure, shown in Fig. 5d for 1L, on the number of layers is also an important consideration, given the nature of the present study. While little experimental information has so far been offered on this matter, our DFT calculations reveal a strong dependence of the band gap energy on the number of hBN layers, changing from 6.1 eV for 1L to 5.6 eV for 6L, as shown in Figure 5e. However, this ~0.5 eV difference originates from the decrease in the CBM with the VBM remaining nearly constant. We therefore do not expect the hBN band gap dependence to affect the tunneling processes here.

We also evaluated the distribution of the applied potential across the graphite/hBN/liquid heterostructure. Fig. 6a shows the difference between the hBN and graphite half-wave potentials

($E_{1/2}^{\text{hBN}}$ and $\overline{E_{1/2}^{\text{gra}}}$, respectively) as a function of the hBN thickness. This difference can be thought of as the additional voltage (akin to an overpotential) that has to be applied, with the hBN barrier present, in order to achieve the same current density as that obtained on bare graphite. We further express this quantity as the fraction of the applied potential "spent" within the hBN, according to the following expression:

$$f_{E,\,1}^{\text{hBN}} = \frac{1}{N} f_{E,\,N}^{\text{hBN}} = \frac{1}{N} \frac{|E_{1/2}^{\text{hBN}} - \overline{E_{1/2}^{\text{gra}}}|}{|E_{1/2}^{\text{hBN}} - E^{0\prime}|} \qquad (10)$$

where $f_{E,\,1}^{\text{hBN}}$ and $f_{E,\,N}^{\text{hBN}}$ are the fractions of E spent per hBN layer and in N layers of hBN, respectively. Fig. 6b shows these fractions as a function of the inverse hBN thickness and, expectedly, suggests that for bulk hBN, $f_{E,\,N}^{\text{hBN}}$ approaches unity for both mediators. However, it also shows that less of E is spent in hBN for $[\text{IrCl}_6]^{3-}$ in comparison to $[\text{Ru}(\text{NH}_3)_6]^{3+}$. This indicates a smaller tunneling barrier for the former, at least for the few-layer hBN measured here, which is in agreement with the differences predicted from Figs. 5b-c.

It is not unlikely that the tunneling transport through hBN is affected by impurity- or defect-induced mid-gap states, as predicted for an hBN/graphene heterostructure[25] and evidenced by a slight p-doping in bulk hBN.[54] Impurities usually average less than 10^{18} cm^{-3} in good quality hBN,[55] which can however be exceeded locally.[56] Our own measurements of bulk hBN and hBN/graphite heterostructure by XPS and Raman spectroscopy, respectively, did not reveal any additional peaks or shoulders in the relevant spectral regions, suggesting that the defect/impurity concentrations are low (Supporting Fig. S4). Furthermore, the dielectric breakdown measurements yielded a high dielectric strength of ~2 V nm^{-1} (Supporting Fig. S5), in agreement with previous reports.[20-22]
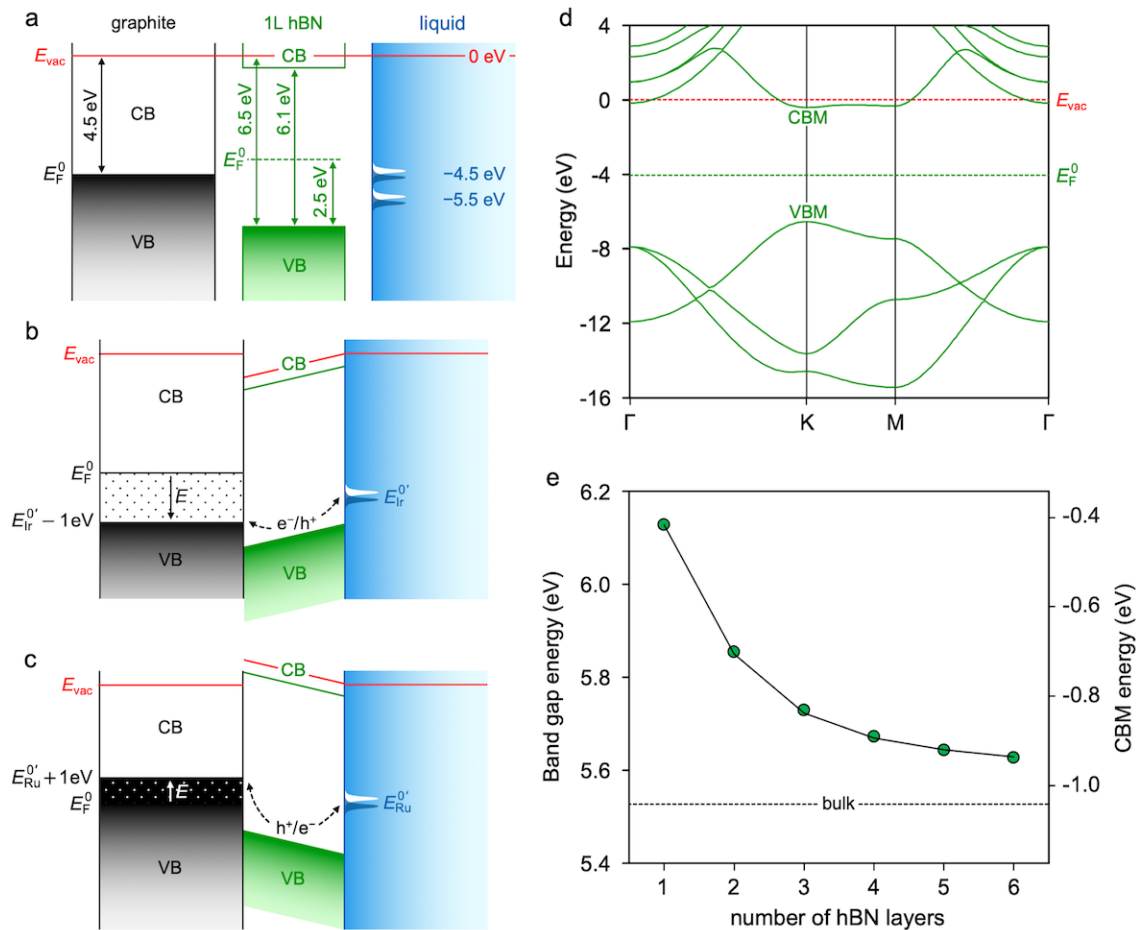
Figure 5 | Band Structure and Alignment of the hBN Tunneling Barrier. a, Band diagram of the different energy levels within the graphite, 1L hBN, and liquid, prior to their contact. **b–c,** Band diagrams of the energy level alignment in the biased graphite/1L hBN/liquid heterostructure for the $[IrCl_6]^{3-}$ oxidation (**b**) and $[Ru(NH_3)_6]^{3+}$ reduction (**c**). **d,** Band structure of 1L hBN. **e,** Evolution of the band gap (circles) and CBM (solid line) on the number of hBN layers. The band gap of bulk hBN, extrapolated from a reciprocal dependence on N, is also shown. Graphite and hBN energy levels and band structures have been calculated using DFT, except for the E_F^0 of hBN, which was taken from ref[54]. The redox energy levels were measured experimentally and converted to a vacuum scale ($E_{vac} = 0$).[57]
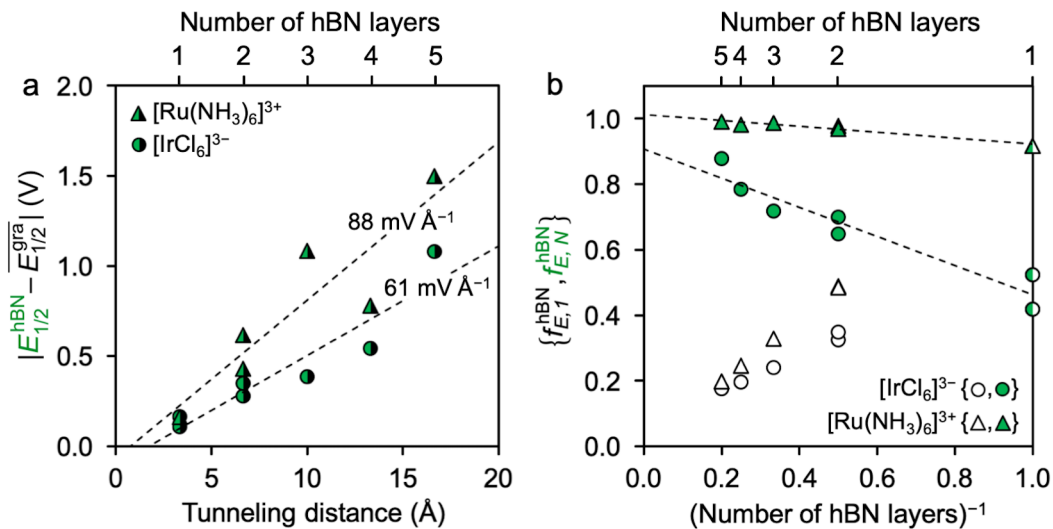
Figure 6 | Applied Potential and Its Distribution Across the Tunneling Barrier. a, Absolute difference between the half-wave potentials on hBN ($E_{1/2}^{\mathrm{hBN}}$) and graphite ($\overline{E_{1/2}^{\mathrm{gra}}}$) as a function of the tunneling distance for both mediators. **b,** Fraction of the applied potential spent within the hBN tunneling barrier for both mediators. Both absolute values (green markers) and values normalized to the hBN thickness (empty markers) are shown.

CONCLUSIONS

We studied electron tunneling across an atomically-flat hBN barrier sandwiched between a graphite electrode and redox levels in a liquid solution. The steady-state voltammetry of $[IrCl_6]^{3-}$ oxidation and $[Ru(NH_3)_6]^{3+}$ reduction obtained on disk ultramicroelectrodes with typical diameters of 5 µm revealed an exponential dependence of the apparent electron transfer rates on the hBN thickness for 1L and 2L hBN. For thicker hBN, deviations in k^0, j_{lim}, and α $(1-\alpha)$ were observed, indicating limitations of the Butler-Volmer model of electrochemical kinetics. We found that this behavior is a direct experimental manifestation of the Marcus-Hush theory, which has been one of the most fundamental treatments of electron transfer. Furthermore, the experimental platform developed here could be exploited in a range of diverse scenarios, including studies of long-range electron transfer, electrochemical switching between outer- and inner-sphere reaction, and electrocatalytic mechanisms. It could be possible to discriminate between outer-sphere and inner sphere reactions as recently shown for 1L MoS_2 on Au,[58] explore electrocatalytic reactions on hBN/metal heterostructures,[59-60] and study proton tunneling/transport through 1L hBN.[61] Such developments are even more likely to succeed, once a reliable control over the thickness and quality of synthetically-grown, large-area hBN is established.[62]

ASSOCIATED CONTENT

Supporting Information.

Tunneling device fabrication; $[IrCl_6]^{2-/3-}$ voltammetry on graphite at varied scan rates; voltammetry in pure supporting electrolyte; Raman spectroscopy and XPS of hBN and graphite; dielectric breakdown estimation.

AUTHOR INFORMATION

Corresponding authors

*matej.velicky@manchester.ac.uk and robert.dryfe@manchester.ac.uk

ORCID

Matěj Velický: 0000-0003-4230-3811

Robert A.W. Dryfe: 0000-0002-9335-4451

Peter S. Toth: 0000-0003-1236-8390

Héctor D. Abruña: 0000-0002-3948-356X

Notes

The authors declare no competing financial interests.

REFERENCES

(1)   Hush, N. S. *Trans. Faraday Soc.* **1961,** *57*, 557-580.

(2)   Marcus, R. A. *Annu. Rev. Phys. Chem.* **1964,** *15*, 155-196.

(3)   Miller, J. R.; Calcaterra, L. T.; Closs, G. L. *J. Am. Chem. Soc.* **1984,** *106*, 3047-3049.

(4)   Chidsey, C. E. D. *Science* **1991,** *251*, 919-922.

(5)   Feldberg, S. W. *Anal. Chem.* **2010,** *82*, 5176-5183.

(6)   Xu, Y.-N.; Ching, W. Y. *Phys. Rev. B* **1991,** *44*, 7787-7798.

(7)   Slonczewski, J. C.; Weiss, P. R. *Phys. Rev.* **1958,** *109*, 272-279.

(8)   Hod, O. *J. Chem. Theory Comput.* **2012,** *8*, 1360-1369.

(9)   Watanabe, K.; Taniguchi, T.; Kanda, H. *Nat. Mater.* **2004,** *3*, 404-409.

(10)   Cassabois, G.; Valvin, P.; Gil, B. *Nat. Photonics* **2016,** *10*, 262-266.

(11)   Mayorov, A. S.; Gorbachev, R. V.; Morozov, S. V.; Britnell, L.; Jalil, R.; Ponomarenko, L. A.; Blake, P.; Novoselov, K. S.; Watanabe, K.; Taniguchi, T.; Geim, A. K. *Nano Lett.* **2011,** *11*, 2396-2399.

(12)   Ahn, G.; Kim, H. R.; Ko, T. Y.; Choi, K.; Watanabe, K.; Taniguchi, T.; Hong, B. H.; Ryu, S. *ACS Nano* **2013,** *7*, 1533-1541.

(13)   Dean, C. R.; Young, A. F.; Meric, I.; Lee, C.; Wang, L.; Sorgenfrei, S.; Watanabe, K.; Taniguchi, T.; Kim, P.; Shepard, K. L.; Hone, J. *Nat. Nanotechnol.* **2010,** *5*, 722-726.

(14)   Bell, R. P., *The Tunnel Effect in Chemistry*. Springer US: 1980; p 222.

(15)   Khairutdinov, R. F.; Zamaraev, K. I.; Zhadanov, V. P., *Electron Tunneling in Chemistry: Chemical Reaction Over Large Distances*. 1st ed.; Elsevier Science: 1989; Vol. 30, p 358.

(16)   Albrecht, T. *Nat. Commun.* **2012,** *3*, 829.

(17)   McCreery, R. L.; Yan, H.; Bergren, A. J. *Phys. Chem. Chem. Phys.* **2013,** *15*, 1065-1081.

(18)   Bard, A. J.; Faulkner, L. R., *Electrochemical Methods. Fundamentals and Applications*. 2nd ed.; John Wiley & Sons, Inc.: New York, 2001.

(19)   Wilt, J.; Gong, Y.; Gong, M.; Su, F.; Xu, H.; Sakidja, R.; Elliot, A.; Lu, R.; Zhao, S.; Han, S.; Wu, J. Z. *Phys. Rev. Appl.* **2017,** *7*, 064022.

(20)   Britnell, L.; Gorbachev, R. V.; Jalil, R.; Belle, B. D.; Schedin, F.; Katsnelson, M. I.; Eaves, L.; Morozov, S. V.; Mayorov, A. S.; Peres, N. M. R.; Castro Neto, A. H.; Leist, J.; Geim, A. K.; Ponomarenko, L. A.; Novoselov, K. S. *Nano Lett.* **2012,** *12*, 1707-1710.

(21)   Britnell, L.; Gorbachev, R. V.; Jalil, R.; Belle, B. D.; Schedin, F.; Mishchenko, A.; Georgiou, T.; Katsnelson, M. I.; Eaves, L.; Morozov, S. V.; Peres, N. M. R.; Leist, J.; Geim, A. K.; Novoselov, K. S.; Ponomarenko, L. A. *Science* **2012,** *335*, 947-950.

(22)   Lee, G.-H.; Yu, Y.-J.; Lee, C.; Dean, C.; Shepard, K. L.; Kim, P.; Hone, J. *Appl. Phys. Lett.* **2011,** *99*, 243114.

(23)   Amet, F.; Williams, J. R.; Garcia, A. G. F.; Yankowitz, M.; Watanabe, K.; Taniguchi, T.; Goldhaber-Gordon, D. *Phys. Rev. B* **2012,** *85*, 073405.

(24)   Chandni, U.; Watanabe, K.; Taniguchi, T.; Eisenstein, J. P. *Nano Lett.* **2015,** *15*, 7329–7333.

(25)   Sachs, B.; Wehling, T. O.; Katsnelson, M. I.; Lichtenstein, A. I. *Phys. Rev. B* **2016,** *94*, 224105.

(26)   Velický, M.; Bradley, D. F.; Cooper, A. J.; Hill, E. W.; Kinloch, I. A.; Mishchenko, A.; Novoselov, K. S.; Patten, H. V.; Toth, P. S.; Valota, A. T.; Worrall, S. D.; Dryfe, R. A. W. *ACS Nano* **2014,** *8*, 10089-10100.

(27)   Wang, L.; Meric, I.; Huang, P. Y.; Gao, Q.; Gao, Y.; Tran, H.; Taniguchi, T.; Watanabe, K.; Campos, L. M.; Muller, D. A.; Guo, J.; Kim, P.; Hone, J.; Shepard, K. L.; Dean, C. R. *Science* **2013,** *342*, 614-617.

(28)   Velický, M.; Bissett, M. A.; Woods, C. R.; Toth, P. S.; Georgiou, T.; Kinloch, I. A.; Novoselov, K. S.; Dryfe, R. A. W. *Nano Lett.* **2016,** *16*, 2023-2032.

(29)   Oldham, K. B.; Zoski, C. G. *J. Electroanal. Chem. Interfacial Electrochem.* **1988,** *256*, 11-19.

(30)   Kresse, G.; Furthmüller, J. *Phys. Rev. B: Condens. Matter Mater. Phys.* **1996,** *54*, 11169-11186.

(31)   Hinuma, Y.; Grüneis, A.; Kresse, G.; Oba, F. *Phys. Rev. B* **2014,** *90*, 155405.

(32)   Heyd, J.; Scuseria, G. E.; Ernzerhof, M. *J. Chem. Phys.* **2006,** *124*, 219906.

(33)   Kretinin, A. V.; Cao, Y.; Tu, J. S.; Yu, G. L.; Jalil, R.; Novoselov, K. S.; Haigh, S. J.; Gholinia, A.; Mishchenko, A.; Lozada, M.; Georgiou, T.; Woods, C. R.; Withers, F.; Blake, P.; Eda, G.; Wirsig, A.; Hucho, C.; Watanabe, K.; Taniguchi, T.; Geim, A. K.; Gorbachev, R. V. *Nano Lett.* **2014,** *14*, 3270-3276.

(34)   Velický, M.; Bissett, M. A.; Toth, P. S.; Patten, H. V.; Worrall, S. D.; Rodgers, A. N. J.; Hill, E. W.; Kinloch, I. A.; Novoselov, K. S.; Georgiou, T.; Britnell, L.; Dryfe, R. A. W. *Phys. Chem. Chem. Phys.* **2015,** *17*, 17844-17853.

(35)   Kneten, K. R.; McCreery, R. L. *Anal. Chem.* **1992,** *64*, 2518-2524.

(36)   Velický, M.; Toth, P. S.; Woods, C. R.; Novoselov, K. S.; Dryfe, R. A. W. *J. Phys. Chem. C* **2019,** *123*, 11677-11685.

(37)   Smalley, J. F.; Feldberg, S. W.; Chidsey, C. E. D.; Linford, M. R.; Newton, M. D.; Liu, Y.-P. *J. Phys. Chem.* **1995,** *99*, 13141-13149.

(38)   Smalley, J. F.; Finklea, H. O.; Chidsey, C. E. D.; Linford, M. R.; Creager, S. E.; Ferraris, J. P.; Chalfant, K.; Zawodzinsk, T.; Feldberg, S. W.; Newton, M. D. *J. Am. Chem. Soc.* **2003,** *125*, 2004-2013.

(39)   Creager, S.; Yu, C. J.; Bamdad, C.; O'Connor, S.; MacLean, T.; Lam, E.; Chong, Y.; Olsen, G. T.; Luo, J.; Gozin, M.; Kayyem, J. F. *J. Am. Chem. Soc.* **1999,** *121*, 1059-1064.

(40)   Sachs, S. B.; Dudek, S. P.; Hsung, R. P.; Sita, L. R.; Smalley, J. F.; Newton, M. D.; Feldberg, S. W.; Chidsey, C. E. D. *J. Am. Chem. Soc.* **1997,** *119*, 10563-10564.

(41)   Bergren, A. J.; McCreery, R. L.; Stoyanov, S. R.; Gusarov, S.; Kovalenko, A. *J. Phys. Chem. C* **2010,** *114*, 15806-15815.

(42)   Ru, J.; Szeto, B.; Bonifas, A.; McCreery, R. L. *ACS Appl. Mater. Interfaces* **2010,** *2*, 3693-3701.

(43)   Yan, H.; Bergren, A. J.; McCreery, R. L. *J. Am. Chem. Soc.* **2011,** *133*, 19168-19177.

(44)   Feldberg, S. W.; Sutin, N. *Chem. Phys.* **2006,** *324*, 216-225.

(45)   Swaddle, T. W. *Chem. Rev. (Washington, DC, U. S.)* **2005,** *105*, 2573-2608.

(46)   Weaver, M. J. *Chem. Rev. (Washington, DC, U. S.)* **1992,** *92*, 463-480.

(47)   Mikkelsen, K. V.; Ratner, M. A. *Chem. Rev. (Washington, DC, U. S.)* **1987,** *87*, 113-153.

(48)   Sutin, N. *Acc. Chem. Res.* **1982,** *15*, 275-282.

(49)   Gerischer, H. *J. Phys. Chem.* **1985,** *89*, 4249-4251.

(50)   Royea, W. J.; Hamann, T. W.; Brunschwig, B. S.; Lewis, N. S. *J. Phys. Chem. B* **2006,** *110*, 19433-19442.

(51)   Sun, P.; Mirkin, M. V. *Anal. Chem.* **2006,** *78*, 6526-6534.

(52)   Slowinski, K.; Slowinska, K. U.; Majda, M. *J. Phys. Chem. B* **1999,** *103*, 8544-8551.

(53)   Miller, C.; Graetzel, M. *J. Phys. Chem.* **1991,** *95*, 5225-5233.

(54)   Henck, H.; Pierucci, D.; Fugallo, G.; Avila, J.; Cassabois, G.; Dappe, Y. J.; Silly, M. G.; Chen, C.; Gil, B.; Gatti, M.; Sottile, F.; Sirotti, F.; Asensio, M. C.; Ouerghi, A. *Phys. Rev. B* **2017,** *95*, 085410.

(55)   Taniguchi, T.; Watanabe, K. *J. Cryst. Growth* **2007,** *303*, 525-529.

(56)   Gibb, A. L.; Alem, N.; Chen, J.-H.; Erickson, K. J.; Ciston, J.; Gautam, A.; Linck, M.; Zettl, A. *J. Am. Chem. Soc.* **2013,** *135*, 6758-6761.

(57)   Trasatti, S. *J. Electroanal. Chem. Interfacial Electrochem.* **1986,** *209*, 417-428.

(58)   Velický, M.; Donnelly, G. E.; Hendren, W. R.; McFarland, S.; Scullion, D.; DeBenedetti, W. J. I.; Correa, G. C.; Han, Y.; Wain, A. J.; Hines, M. A.; Muller, D. A.; Novoselov, K. S.; Abruña, H. D.; Bowman, R. M.; Santos, E. J. G.; Huang, F. *ACS Nano* **2018,** *12*, 10463-10472.

(59)   Uosaki, K.; Elumalai, G.; Noguchi, H.; Masuda, T.; Lyalin, A.; Nakayama, A.; Taketsugu, T. *J. Am. Chem. Soc.* **2014,** *136*, 6542-6545.

(60)   Liu, D.-Q.; Tao, B.; Ruan, H.-C.; Bentley, C. L.; Unwin, P. R. *Chem. Commun. (Cambridge, U. K.)* **2019,** *55*, 628-631.

(61)   Hu, S.; Lozada-Hidalgo, M.; Wang, F. C.; Mishchenko, A.; Schedin, F.; Nair, R. R.; Hill, E. W.; Boukhvalov, D. W.; Katsnelson, M. I.; Dryfe, R. A. W.; Grigorieva, I. V.; Wu, H. A.; Geim, A. K. *Nature* **2015,** *516*, 227-230.

(62)   Wang, L.; Xu, X.; Zhang, L.; Qiao, R.; Wu, M.; Wang, Z.; Zhang, S.; Liang, J.; Zhang, Z.; Zhang, Z.; Chen, W.; Xie, X.; Zong, J.; Shan, Y.; Guo, Y.; Willinger, M.; Wu, H.; Li, Q.; Wang, W.; Gao, P.; Wu, S.; Zhang, Y.; Jiang, Y.; Yu, D.; Wang, E.; Bai, X.; Wang, Z.-J.; Ding, F.; Liu, K. *Nature* **2019,** *570*, 91-95.
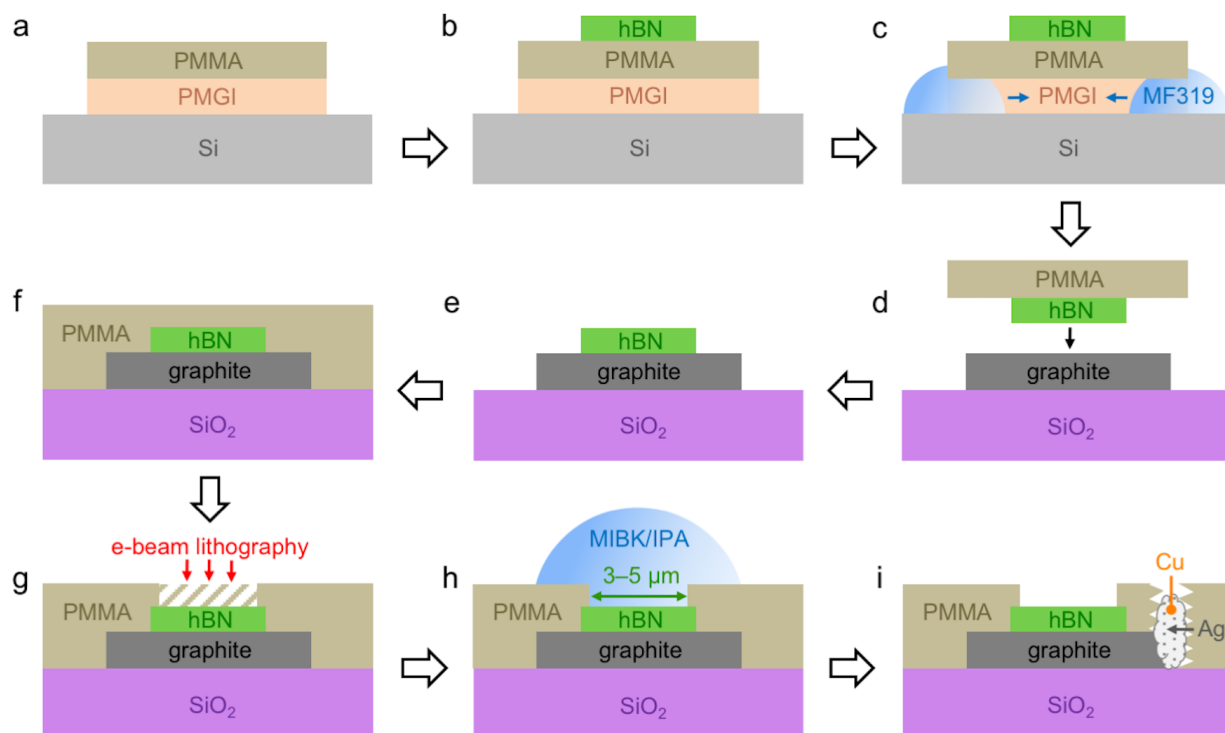
Supporting Information:

Marcus-Hush Theory Revealed by Electron Tunneling

Through Hexagonal Boron Nitride

Matěj Velický,*[1,2,3] Sheng Hu,[2] Colin R. Woods,[2] Peter S. Toth,[1,4] Viktor Zólyomi,[2] Andre K. Geim,[2] Héctor D. Abruña,[3] Kostya S. Novoselov,[2] and Robert A. W. Dryfe*[1]

[1] School of Chemistry and [2] School of Physics and Astronomy, University of Manchester, Oxford Road, Manchester, M13 9PL, United Kingdom

[3] Department of Chemistry and Chemical Biology, Cornell University, Ithaca, New York, 14853, United States

[4] MTA Premium Post Doctorate Research Program, Department of Physical Chemistry and Materials Science, University of Szeged, Rerrich Square 1, Szeged H-6720, Hungary

Supporting Figure S1│ Schematic of the Tunneling Device Fabrication. a, Polydimethylglutarimide (PMGI) first and PMMA second were spin-coated onto a Si wafer. **b,** hBN was exfoliated on a PMMA/PMGI/Si substrate. **c,** PMGI was dissolved using MF 319 (2.45% tetramethylammonium hydroxide in water). **d,** PMMA/hBN stack was transferred onto graphite, which was previously exfoliated onto a 300 nm SiO$_2$/Si wafer. **e,** PMMA is peeled away, while hBN remains on graphite, held by vdW forces (**c–e** loosely follows the "dry-peel" stamp-transfer method described in ref.[1]). **f,** PMMA was spin-coated (130 nm thickness, measured by profilometry) onto the hBN/graphite heterostructure. **g,** e-beam lithography is used to define a circular opening (3–5 μm in diameter) in PMMA. **h,** irradiated PMMA photoresist was dissolved with methyl isobutyl ketone/isopropanol (MIBK/IPA). **i,** PMMA was mechanically scratched 300–500 μm away from the opening and the freshly-exposed graphite was contacted using a Ag paint and a Cu wire.
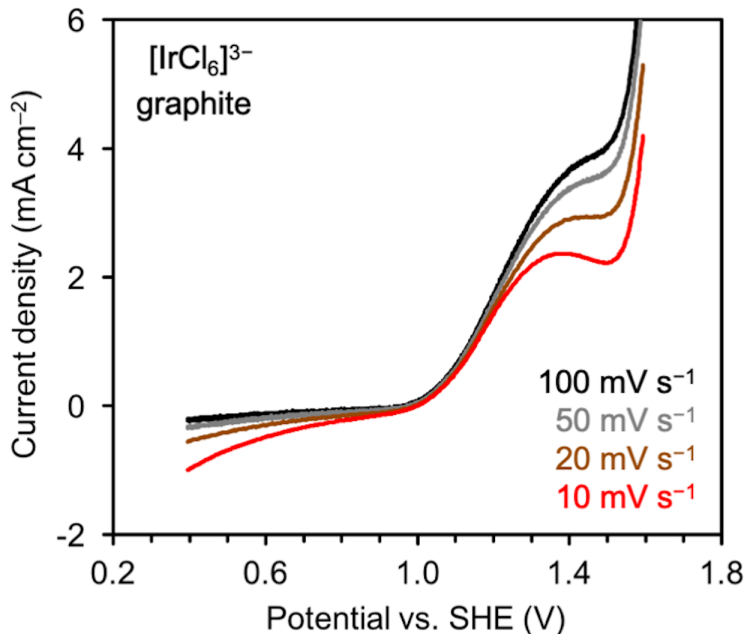
Supporting Figure S2 | Voltammetry of $[IrCl_6]^{3-}$ Oxidation on Graphite. A steady-state voltammogram of an ultramicroelectrode under a radial diffusion regime is independent of the scan rate. The differences between the voltammograms recorded at different scan rates in this figure arise from the fact that, for scan rates slower than 100 mV s^{-1}, the diffusion layer thickness become comparable to the dimensions of the microdroplet electrochemical cell, which leads to the thin-layer cell diffusional effects. Conversely, faster scans result in a deviation from the steady-state due to the increasing contributing from the linear diffusion. Scanning at 100 mV s^{-1} yields >95 % steady-state microelectrode response, considering the electrode radius (2.5 μm) and the diffusion coefficient of $[IrCl_6]^{3-}$ (2.1 × 10^{-6} cm^2 s^{-1}),[2] and was therefore chosen as a good compromise to achieve the steady-state response, while avoiding the undesirable thin-layer cell effects. The limiting current (I_{lim}) obtained on graphite at 100 mV^{-1} was generally found to be in agreement with the theoretical value for a disk ultramicroelectrode ($I_{lim} = 4nFDcr$, where n is the number of electron transferred, F is the Faraday constant, D is the diffusion coefficient of the mediator, c is the mediator concentration, and r is the radius of the microelectrode).[3] I_{lim} was within 15% of the theoretical value for $[IrCl_6]^{3-}$ (a slight increase was observed due to the convolution with surface oxidation at high potentials) and within 5% for $[Ru(NH_3)_6]^{3+}$. The PMMA recess plays a negligible role in the diffusional regime since its height (130 nm) is about 5% of the electrode radius.[4]
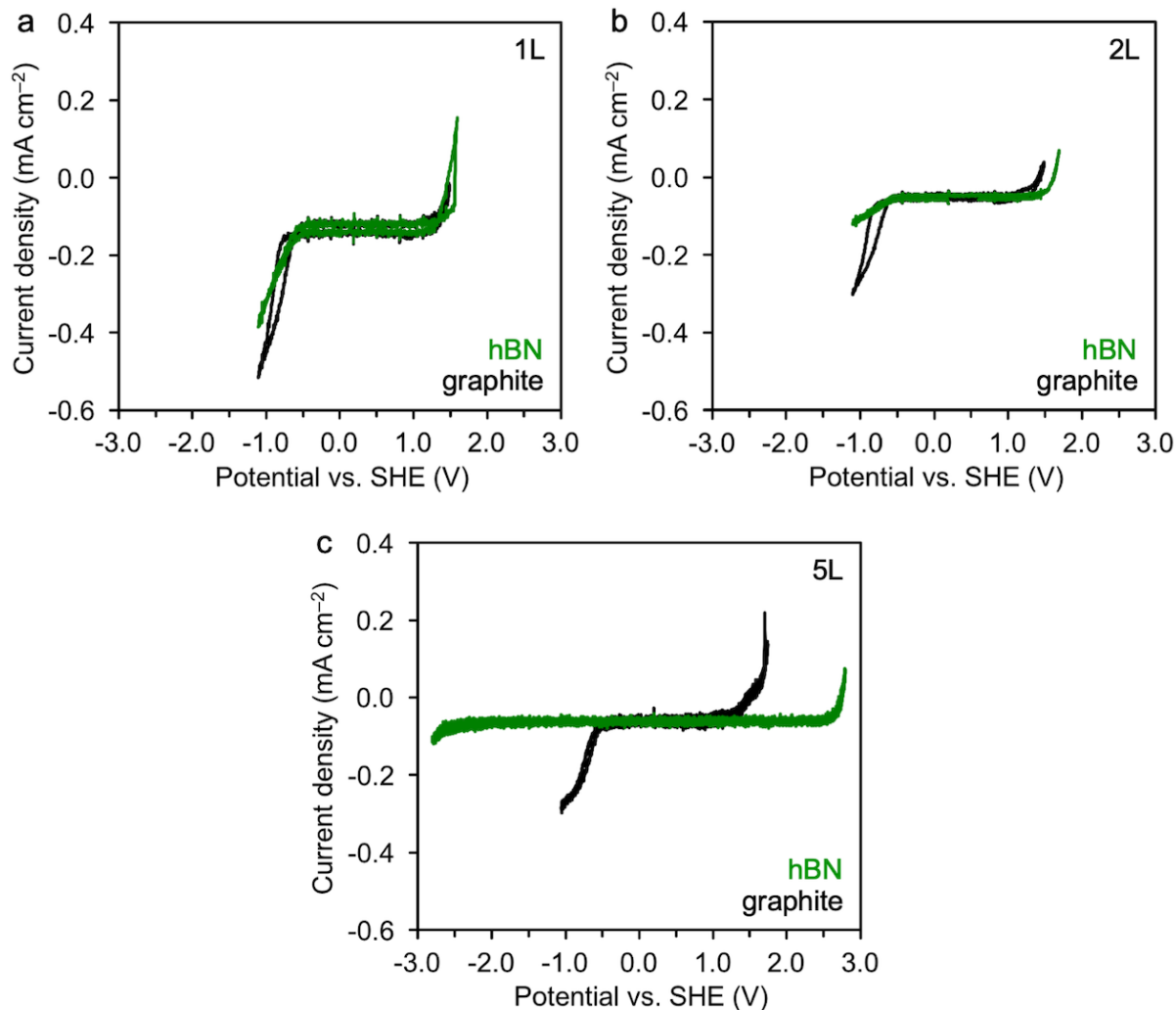
Supporting Figure S3│ Voltammetry in the 6 M LiCl Supporting Electrolyte. Cyclic voltammograms on hBN (green curves) and bare graphite (black curves), demonstrating how the potential window widens with increasing hBN thickness, due to a reduction in the electron transfer rate of the side-reactions delimiting the window at the potential extremes. Data for 1L (**a**), 2L (**b**), and 5L (**c**) hBN are shown.
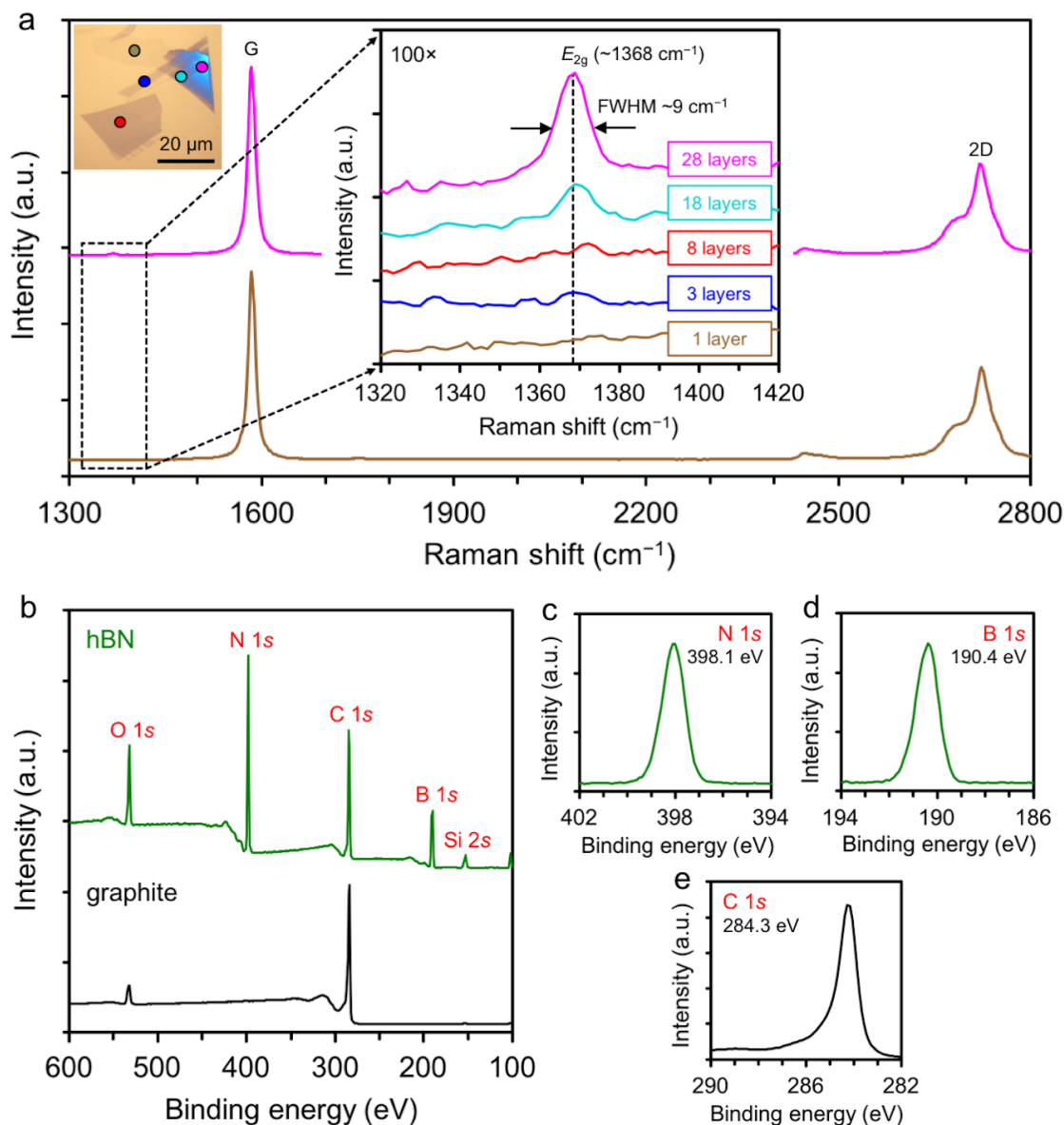
Supporting Figure S4 │ Raman Spectroscopy and XPS of hBN and Graphite. a, Raman spectra of hBN on graphite. The presence of the E_{2g} mode at ~1368 cm^{-1} confirms the hexagonal phase of hBN,[5] but its intensity in 1L and few-layer hBN is negligible in comparison to the G and 2D modes in graphite/graphene and therefore prevent detailed analysis.[6] In order to avoid laser-induced damage, the Raman spectra were acquired after the electrochemical measurements. Top-left inset: an optical image of the different hBN layers showing the collection spots. **b,** Survey XPS spectra of bulk hBN (top) and graphite (bottom). **c–e,** High-resolution XPS spectra of the N 1*s*, B 1*s*, and C 1*s* regions, showing single Gaussians without shoulders for N and B at expected binding energies and FWHM ~1 eV, indicating low concentration of impurities in hBN.[5] The C 1*s* binding energy corresponds to the sp^2 carbon hybridization and contains a shoulder at the high-energy tails, indicating partial surface oxidation common in graphite.[7] The XPS quantification was not considered reliable due to the low XPS sensitivity for light elements.
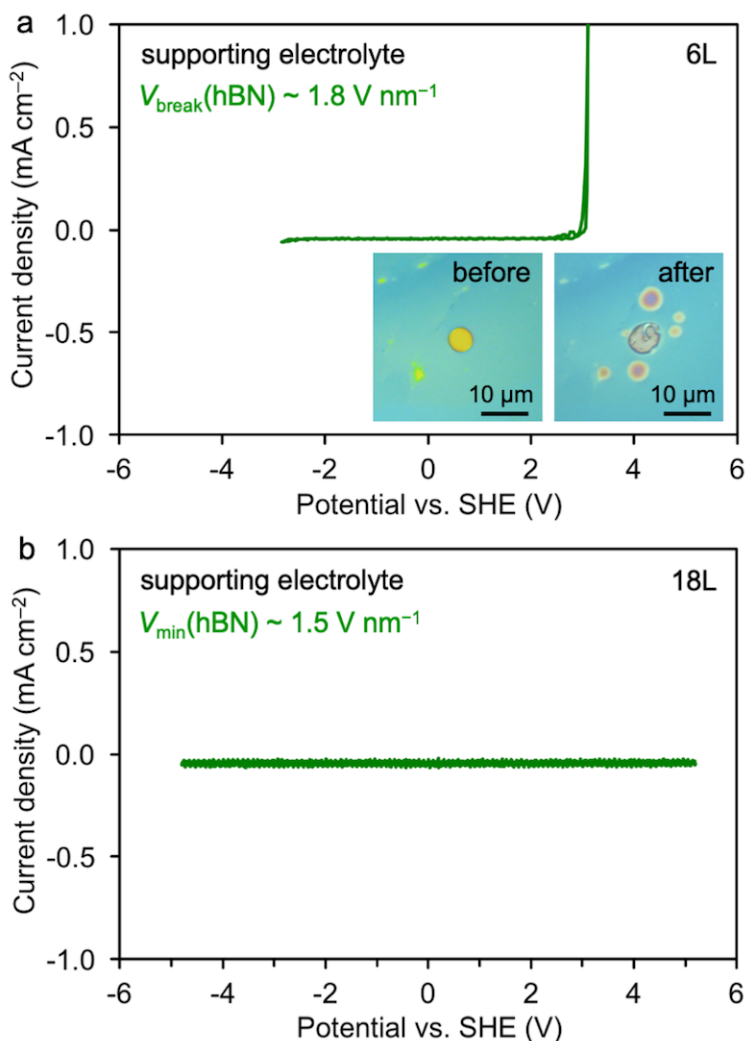
Supporting Figure S5 │ Dielectric Breakdown Estimation. Voltammetry in 6 M LiCl electrolyte for 6L (**a**) and 18L (**b**) hBN. The thinner 6L hBN (which also included a contamination layer trapped between the hBN and graphite) underwent dielectric breakdown upon applied voltage of ~ 6 V. The thicker 18L hBN withstood an applied voltage of ~ 10 V. This yields an average estimate of ~2 V nm^{-1} (GV m^{-1}) for the hBN dielectric breakdown, based on the AFM-measured hBN thickness and assuming a linear electric field. The insets in **a** show the optical micrograph of the hBN opening in the PMMA, before and after the dielectric breakdown. Previous publications reported similar dielectric strength, and showed higher susceptibility of thicker (>9 nm) hBN to dielectric breakdown.[8-10] Indeed, we found that all of our hBN crystals thicker than ~15 nm "leaked" current.

References

1.   Wang L*., et al.* One-Dimensional Electrical Contact to a Two-Dimensional Material. *Science* **342**, 614-617 (2013).
2.   Aoki K., Akimoto K., Tokuda K., Matsuda H.& Osteryoung J. Linear sweep voltammetry at very small stationary disk electrodes. *J. Electroanal. Chem.* **171**, 219-230 (1984).
3.   Bard A. J.& Faulkner L. R. *Electrochemical Methods. Fundamentals and Applications*, 2nd edn. John Wiley & Sons, Inc. (2001).
4.   Bond A. M., Luscombe D., Oldham K. B.& Zoski C. G. A comparison of the chronoamperometric response at inlaid and recessed disc microelectrodes. *J. Electroanal. Chem. Interfacial Electrochem.* **249**, 1-14 (1988).
5.   Henck H*., et al.* Direct observation of the band structure in bulk hexagonal boron nitride. *Phys. Rev. B* **95**, 085410 (2017).
6.   Gorbachev R. V*., et al.* Hunting for monolayer boron nitride: Optical and raman signatures. *Small* **7**, 465-468 (2011).
7.   Velický M*., et al.* Electron Transfer Kinetics on Mono- and Multilayer Graphene. *ACS Nano* **8**, 10089-10100 (2014).
8.   Britnell L*., et al.* Electron tunneling through ultrathin boron nitride crystalline barriers. *Nano Lett.* **12**, 1707-1710 (2012).
9.   Britnell L*., et al.* Field-Effect Tunneling Transistor Based on Vertical Graphene Heterostructures. *Science* **335**, 947-950 (2012).
10.   Lee G.-H*., et al.* Electron tunneling through atomically flat and ultrathin hexagonal boron nitride. *Appl. Phys. Lett.* **99**, 243114 (2011).